Evidence for synergy between sarcomeres and fibroblasts in an in vitro model of myocardial reverse remodeling

Shi Shen M.S.[1], Lorenzo R. Sewanan, Ph.D.[1], Stuart G. Campbell, Ph.D.[1,2]

1. Department of Biomedical Engineering, Yale University, New Haven, CT, USA
2. Department of Cellular and Molecular Physiology, Yale School of Medicine, New Haven, CT, USA

For Correspondence:
Dr. Stuart G. Campbell, PhD
stuart.campbell@yale.edu
55 Prospect St.
New Haven, CT 06511

Abstract

We have created a novel in-vitro platform to study reverse remodeling of engineered heart tissue (EHT) after mechanical unloading. EHTs were created by seeding decellularized porcine myocardial sections with a mixture of primary neonatal rat ventricular myocytes and cardiac fibroblasts. Each end of the ribbon-like constructs was fixed to a plastic clip, allowing the tissues to be statically stretched or slackened. Inelastic deformation was introduced by stretching tissues by 20% of their original length. EHTs were subsequently unloaded by returning tissues to their original, shorter length. Mechanical characterization of EHTs immediately after unloading and at subsequent time points confirmed the presence of a reverse-remodeling process, through which stress-free tissue length was increased after chronic stretch but gradually decreased back to its original value within nine days. When a cardiac myosin inhibitor was applied to tissues after unloading, EHTs failed to completely recover their passive and active mechanical properties, suggesting a role for actomyosin contraction in reverse remodeling. Selectively inhibiting cardiomyocyte contraction or fibroblast activity after mechanical unloading showed that contractile activity of both cell types was required to achieve full remodeling. Similar tests with EHTs formed from human induced pluripotent stem cell-derived cardiomyocytes also showed reverse remodeling that was enhanced when treated with omecamtiv mecarbil, a myosin activator. These experiments suggest essential roles for active sarcomeric contraction and fibroblast activity in reverse remodeling of myocardium after mechanical unloading. Our findings provide a mechanistic rationale for designing potential therapies to encourage reverse remodeling in patient hearts.

Key Words: Myocardial remodeling; sarcomere; mechanotransduction; engineered heart tissue

Abbreviations

α-SMA- alpha-smooth muscle actin

cTnT- cardiac troponin T

DC- drug control

DCM- dilated cardiomyopathy

DIRR- double-inhibited reverse remodeling

DT- destination therapy

ECM- extracellular matrix

EHT- engineered heart tissue

FIRR- fibroblast-inhibited reverse remodeling

Ctrl- Control group

HCF- human cardiac fibroblast

HF- heart failure

hiPSC-CMs- human induced pluripotent stem cell-derived cardiomyocytes

IHC- immunohistochemistry

LVAD- left ventricular assist device

LVEF- left ventricular ejection fraction

MMP- matrix metalloproteinase

NRVMs- neonatal rat ventricular myocytes

NRCFs- neonatal rat cardiac fibroblasts

OM – Omecamtiv Mecarbil

OCT- optical coherence tomography

PF- peak fore

REMATCH- randomized evaluation of mechanical assistance for the treatment of congestive heart failure

RR- reverse remodeling

RT50- time to 50% relaxation from the peak

SIRR- sarcomere-inhibited reverse remodeling

TGF-β- Transforming growth factor- β

TIMP- tissue inhibitors of metalloproteinase

TTP- time to peak

Introduction

The left ventricular assist device (LVAD) has emerged as a life-saving treatment option for many advanced heart failure (HF) patients [1–5]. The shift in usage of LVAD from short-term to long-term therapy is reflected in the national statistics; among over 15,000 LVADs implanted between 2006 to 2014, the percentage of LVADs implanted for destination therapy increased from 14.7% to 45.7% [6]. Among the patients receiving an LVAD, most experience some degree of recovery in cardiac function, while a small number undergo more significant functional, structural, and cellular improvement in a process called reverse remodeling (RR) [7–9].

Reverse remodeling is an intrinsic tissue-level process that results in restoration of normal cardiomyocyte size and extracellular matrix composition as well as reductions in inflammation and pro-apoptotic signaling [8,10]. This recovery process enables some patients to regain sufficient cardiac function to allow LVAD explantation, prompting the notion of LVAD as bridge to recovery therapy [8,10,11]. However, the number of adult nonischemic dilated cardiomyopathy (DCM) patients experiencing recovery following LVAD support is relatively small [8,10,12–17], with overall LVAD explanation rate observed to be around 5% [12,13]. Moreover, since DCM is the most common form of cardiomyopathy in children [6], LVADs have also been often used in pediatric patients with advanced HF from DCM [18–20]. Similar trends but higher recovery have been reported, with even better outcome observed for children less than two years old [19].

It is not fully understood why mechanical unloading leads to recovery of cardiac function and HF remission only in certain patients. A major obstacle is a lack of understanding about the mechanisms that drive reverse remodeling on a cell and tissue level. Until these mechanisms are identified and described, the path toward encouraging beneficial remodeling after myocardial unloading will remain obscure.

Here, we describe the development of a novel *in vitro* model that enables study of the basic phenomenon of myocardial reverse remodeling after mechanical unloading. Using our engineered heart tissue (EHT) platform and a custom stretch device, we first overloaded tissues

by subjecting them to two days of stretch. We could then 'unload' EHTs and observe the reverse remodeling process in detail, enabling the identification of specific cellular and molecular contributors. These findings provide the first description of a novel platform for studying the fundamental processes involved in myocardial reverse remodeling and may inspire future therapeutic strategies for diseases that feature cardiac chamber dilation.

Methods

Ethical Approval

Animal procedures were all approved by the Yale University Institutional Animal Care and Use Committee (Approval # 2018-11528), and compliant with the regulations of the Animal Welfare Act, Public Health Service, the United States Department of Agriculture, and the principles and regulations of the Journal of Physiology [21]. 1-2-day old Sprague-Dawley neonatal rat litters used for this study were purchased from Charles River Laboratories (Wilmington, MA). The animals were kept under a 12-hour light/dark cycle with constant access to water and food pellets. Neonatal rats were anesthetized for 10 minutes under 500mL/min oxygen with 3% isoflurane until the animals were completely unresponsive to physical stimulation prior to decapitation and removal of whole hearts.

Reagents

Cardiomyocyte primary isolation kit, modified eagle medium (DMEM), Dulbecco's phosphate-buffered saline (DPBS), horse serum (HS), fetal bovine serum (FBS), and penicillin-streptomycin (P/S) were purchased from ThermoFisher Scientific. L-ascorbic acid, insulin solution, and Pluronic F-127 were from Sigma Aldrich. Mavacamten (MYK-461), SB-431542, and Omecamtiv mecarbil were purchased from Cayman Chemical. Hank's balanced salt solution (HBSS) was obtained from Gibco. Rat BNP 45 ELISA kit and soluble collagen assay kit were from Abcam.

EHT Production

Decellularized scaffolds were produced as previously described (Figure 1A) [22]. Briefly, fresh pig hearts were purchased from J Latella & Sons (West Haven, CT) and preserved in ice

cold DPBS with 5% P/S during transport. Left ventricular free wall portion of the hearts were then trimmed, cut into blocks, and frozen in dry ice. 150µm-thick longitudinal slices were obtained from the frozen heart blocks with a cryostat microtome (Leica CM3050 S). Slices were then laser cut (1mm x 6mm) and incubated in lysis buffer with 10mM Tris and 0.1% 0.5M EDTA. EHT holders were also laser cut from Teflon and autoclaved before assembling the laser-cut scaffold onto the holders. Scaffolds were then decellularized in 0.5% wt/vol sodium dodecyl sulfate in DPBS and incubated overnight in media with DMEM, 10% FBS, and 2% P/S before seeding.

Neonatal cardiac cell isolation

The atrial portion was trimmed from hearts and the remaining ventricular tissue was sliced into small chunks with a surgical scalpel and digested with enzymes from the isolation kit. Digested cell suspensions were gently homogenized and plated for two hours to remove debris and excessive cardiac fibroblasts before cell counting and seeding. One million cells were seeded per tissue in 50 µL seeding volume with seeding media composed of DMEM, 10% FBS, and 1% P/S. After seeding, media was changed every other day with rat maintenance media made of DMEM, 10% HS, 2% FBS, 1 µL/mL insulin solution, and 5 µL/mL L-ascorbic acid from 10mg/mL stock prepared in DPBS. Tissues were observed for appropriate cell attachment and synchronous contraction for 7 days before experiments.

Human induced pluripotent stem cell-derived cardiomyocyte (hiPSC-CM) differentiation

A healthy control stem cell line (GM23338, Coriell Institute) was maintained in mTeSR media (STEMCELL Technologies) until close to 100% confluency. A standard differentiation protocol was used [23]. Briefly: 15 µM chiron (CHIR99021, STEMCELL Technologies) was added on day 0 for 24 hours and 5 µM IWP4 (STEMCELL Technologies) was added on day 3 for 48 hours. The cells were cultured in RMPI supplemented with B27 (minus insulin, Thermofisher) until day 9 when the supplement was changed to B27 Plus (with insulin, Thermofisher). 4-day 4 mM lactate selection from day 12 helped purify the hiPSC-CMs before cells were seeded on day 18. For EHT seeding, a total of one million cells was seeded per tissue, with 80% hiPSC-CMs and 20% adult human cardiac fibroblasts (306-05A, PromoCell). Seeding media was made of DMEM, 10% FBS, 1% P/S, 1% non-essential amino acids, 1% L-glutamine,

and 1% sodium pyruvate. After seeding, the tissues were maintained in DMEM with B27 Plus supplement and media was changed every other day. Appropriate cell attachment and synchronous contraction were monitored for 7 days before experiments.

Immunohistochemistry

Tissues were fixed in formalin (Sigma) for 15 min and washed with DPBS three times before storing in 70% ethanol. The tissues were blocked with 3% BSA in DPBS for one hour before incubating with mouse anti-cardiac troponin T (cTnT, MA5-12960, Invitrogen) and rabbit anti-alpha smooth muscle actin (α-SMA, EPR5368, Abcam) primary antibodies overnight. Tissues were then incubated for 1hr with anti-rabbit Alexa Fluor 488 and anti-mouse Alex Fluor 647 secondary antibodies (Thermofisher) before mounting onto glass slides with antifade mountant and DAPI (P36962, Invitrogen). Tissues were imaged on a Leica confocal microscope.

Novel EHT stretching device

A novel device was designed and constructed, consisting of assembled laser-cut PTFE (Teflon) parts. Each device is designed to stretch a single EHT and can fit into individual wells on a 6-well plate (Figure 1B). It contains a pair of irregular octagons that press against a flexible Teflon retainer that fits the clip attached to one end of the tissue. When the octagons are turned stepwise to 45 and 90 degrees with a pair of tweezers, the tissue is stretched by 10% and 20% respectively. The device was used to stretch individual tissues to 10% for 24 hours, and 20% for another 24 hours before unloading (Figure 1C).

EHT biomechanical testing and analysis

A custom mechanical measurement system was used to investigate the biomechanical properties of EHTs. Clips holding either end of the tissue are mounted onto custom hooks. One hook is affixed to a force transducer, and the other to a linear actuator, enabling the force-length characterization of the EHT. A custom 3D-printed bath integrated with printed circuit board and platinum wires was used to provide temperature control and electrical stimulation during testing. The bath also contained inlet and outlet flow channels connected to syringe pumps to enable continuous perfusion of testing solution. Tyrode's solution was used as the testing solution throughout the experiments (in mM: 140 NaCl, 5.4 KCl, 1.8 $CaCl_2$, 1 $MgCl_2$, 25 HEPES, and 10

glucose; pH 7.3). Custom MATLAB scripts were used to record the raw mechanical data of both active twitches and passive forces during isometric stretch and electrical pacing. To measure tissue slack length, the point at which the tissue starts to develop passive force, and tissue stiffness among other passive mechanics properties, an isometric stretch protocol was used to stretch the tissue from 85% culture length to 110% culture length (10% stretch relative to culture length) at 1Hz constant pacing. The entire stretch sequence containing both passive and active forces was recorded and repeated (Figure 1D). Active twitches were recorded three separate times while tissues were held isometrically at 10% stretch. Optical coherence tomography was used after mechanical testing to measure the cross-sectional area of the tissues (Figure 1E). Automated MATLAB scripts were used to manage metadata and analyze raw mechanical data. Cross-sectional areas, slack length, tissue stiffness and other passive mechanics properties were obtained with automated scripts from normalized passive data against cross-sectional areas (Figure 1F) as previously described [24]. Active data including peak force, time to peak (TTP), time to 50% relaxation (RT50) were derived from active force data (Figure 1G) as averages across all repeated recordings. Graphpad Prism 8 software was used for data visualization.

Preparation of drug-supplemented culture media

Mavacamten and SB-431542 were reconstituted in dimethyl sulfoxide (DMSO) at 1mM and 5mg/mL stock solutions respectively and frozen as aliquots. Media containing either mavacamten or SB-431542 were prepared fresh for every media change. To prepare the media, mavacamten and SB-431542 aliquots were directly added into the media to achieve 500nM and 10μM concentrations respectively before sterile filtration. Mavacamten and SB-431542 contributed to 0.05% and 0.077% DMSO (v/v) in the culture media. The DMSO concentrations from the two drugs were only 2% and 3% of what was reported to induce noticeable effects on cardiomyocytes [25].

Statistical methods

To compare the mechanical properties between the two groups in the initial reverse remodeling characterization experiment, two-tailed unpaired t test was used ($n \geqslant 3$ for all groups). Non-linear regression with one-phase decay was used to analyze the reverse remodeling profile over time in our system. The subsequent SB-431542 control experiment used two-tailed unpaired t tests, two-way ANOVA with repeated measures, and linear regression to analyze the data (both control and treatment groups $n \geqslant 10$). 3-way ANOVA with planned comparisons were used to examine the significance of active contraction inhibition and to assess the differences between select groups (all groups $n \geqslant 7$). For the experiment investigating the interaction between cardiomyocytes and cardiac fibroblasts in the reverse remodeling process, 3-way ANOVA with repeated measures, 2-way ANOVA with planned comparisons or Tukey's post hoc tests among the groups, and linear regression analysis were used (all groups $n \geqslant 9$). Due to ANOVA's sensitivity to outliers, one outlier with over 2.5 times of standard deviation was excluded from the SIRR group. Linear correlations were performed to assess the relationship between active and passive mechanical properties of reverse remodeled tissues. 2-way ANOVA with repeated measures and two-tailed unpaired t tests were conducted for follow-up human EHT-based experiments. All analysis was performed in Graphpad Prism 8 software, and the data were presented in the form of mean and standard deviation wherever possible. A $P < 0.05$ was used for interactions among all groups to be considered significant.

Results

In vitro model validation

We sought a system in which a linear segment of artificial myocardium could first be stretched to the point of inelastic (not immediately reversible) deformation. We hypothesized that relieving tension in this over-stretched tissue would provide an opportunity to study the reverse remodeling process in detail, by monitoring biomechanical characteristics of the engineered heart tissues (EHTs), including stress-free tissue length (slack length), stiffness, and active contractile force during a recovery interval. Recovery of the slack length to its original value was considered the functional endpoint marking completion of reverse remodeling.

An initial reverse remodeling experiment was performed to compare the mechanical properties between the control group (Ctrl), which was not stretched, and the reverse remodeling (RR) group, which underwent static stepwise stretch to 20% over 48 hours followed by unloading (return to 0% stretch; Figure 2A).

To avoid tissue damage during acute stretch, EHTs in the RR group were treated during the stretch interval with the cardiac-specific myosin inhibitor mavacamten. The tissues from both groups were tested around the same time, with RR tissues all tested immediately after mechanical unloading and every day up to 12 days following unloading. Mechanical testing showed that immediately after unloading, normalized passive forces were significantly different between the two groups, with RR tissues developing less passive stress at high stretch percentage compared with Ctrl tissues (Figure 2B, 2-way ANOVA with repeated measures $P < 0.0001$). RR group tissues also had significantly increased cross-sectional areas compared with Ctrl group tissues (Figure 2C, $P = 0.0105$, effect size = 3.3). The increase in slack length in RR group tissues was also significant (Figure 2D), indicating that our device effectively exposed tissues to inelastic deformation that was not immediately reversible ($P = 0.0131$, effect size = 3.1). Tissue stiffness analysis demonstrated that Ctrl tissues possessed physiological stiffness, around 10 kPa at 0% stretch [26]. Stiffness of RR tissues immediately after unloading was markedly reduced over a 0-7% stretch range (Figure 2E) and retained only 13% stiffness of Ctrl tissues at culture

length. RR tissues also had a 60% drop in normalized peak force production at 1 Hz pacing compared with Ctrl tissues (Figure 2F, P = 0.0152).

In addition, BNP-45 level in cell culture media was measured and showed a 41% increase in RR tissue media after 48-hour stretch compared with those in Ctrl tissue media (Figure 2G). Furthermore, soluble collagen levels in cell culture medium revealed a 112% increase in newly synthesized collagen in RR tissues media after 48-hour compared with those of Ctrl tissues (Figure 2H). This spike in soluble collagen production was temporally consistent with a previously reported human fibroblast study [27]. Collectively, the stepwise static stretch with mavacamten incubation resulted in significant diastolic and systolic dysfunction (Figure 2B-F) along with indications of biological stress (Figure 2G) and heightened fibroblast activity (Figure 2H).

After unloading, RR tissues' reverse remodeling behaviors were characterized. First, BNP 45 level measured at one day after unloading showed significant reduction in RR tissue media compared with those in Ctrl tissues (Figure 2I, P = 0.0344). Second, between days 0 and 9 after unloading, the soluble collagen assay revealed a 50% drop in new collagen synthesis in RR tissue media while levels in Ctrl tissues remained the same (Figure 2H, 2J).

A time-course study was carried out next to characterize the slack length change in RR tissues across 12 days after mechanical unloading. Two RR tissues were tested each day post-unloading, and the resulting slack lengths were plotted on a continuous timeline as a measure of the degree of reverse remodeling of the EHTs (Figure 2K). Using a decaying exponential model to fit the data, the time constant of reverse remodeling was ~2.2 days (R^2 = 0.7185), with the slack length reaching a plateau around nine days after unloading. Therefore, to capture the reverse remodeling progression in subsequent experiments, EHT mechanics were measured at day 1 and day 9 post-unloading. Moreover, to examine the recovery of both diastole and systolic function of RR tissues during reverse remodeling, RR tissue cross-sectional area, stiffness at 7% stretch, and normalized peak force at 1Hz pacing were also plotted on the same time axis (Figure 2L, 2M, 2N). Significant linear correlations were observed for all three- tissue cross-sectional area (P

= 0.0013), tissue stiffness (P = 0.0007) and peak stress (0.0033), validating the presence of reverse remodeling in both passive and active mechanics in our *in-vitro* model.

To visualize the distribution and morphology of the different cell types, an RR tissue 9 days after unloading was fixed and imaged for cTnT (Figure 2O), α-SMA (Figure 2P), and DAPI (Figure 2Q). IHC images showed visible cell infiltration throughout the entire decellularized scaffold, relatively uniform distribution of cardiomyocyte sarcomeres (red) and the presence of activated myofibroblasts with stress fibers (in green, Figure 2R). The artifacts of high fluorescence intensity near the tissue edges are most likely a result of heat effects on the scaffold margins during laser cutting.

In order to confirm that the changes in slack length seen after unloading were being driven by active cellular processes, we subjected decellularized, un-seeded myocardial scaffolds to the same stretch-unloading protocol as in the case of seeded constructs (Figure 3A). Scaffolds undergoing 20% stretch experienced a ~15% increase in slack length that did not recover, even when left for six days in culture (Figure 3B). Stiffness of the stretched samples was negligible in comparison to unstretched decellularized tissues, suggesting inelastic deformation of the matrix as a consequence of 20% stretch (Figure 3C).

Role of cardiac fibroblasts in remodeling the tissue matrix in an EHT system

Since cardiac fibroblasts play a key role in maintaining and remodeling the ECM, we investigated the contribution of fibroblasts on matrix remodeling in our EHTs via the modulation of the TGF-β canonical signaling pathway. Two groups with four EHTs each were seeded with NRVMs and NRCFs as before, with 10μM of the TGF-β1 inhibitor SB-431542 added to the treatment group the day after seeding. Brightfield images were recorded every day for both groups at 4x magnification. The degree of tissue remodeling was quantified by measuring the width of each tissue at its midline over several days of remodeling (Figure 4A). After eight days, SB-431542 was removed from the treatment group, and images were recorded until day 14. Images showed significantly reduced remodeling for tissues treated with SB-431542 when compared with the control group (Figure 4A, effect size = 1.9). Moreover, the inhibition of fibroblast activity was reversible since the treated tissues resumed remodeling after drug removal

and reached an end-stage remodeling by day 14 that was similar to control tissues on day 8 (Figure 4B).

SB-431542 has been used to inhibit canonical TGF-β1 signaling in multiple cell types, including cardiac fibroblasts [28–30]. As such, we considered the possibility that it could functionally affect cardiomyocytes in our EHTs, rather than specifically targeting fibroblasts. Therefore, a SB-431542 control experiment was next carried out to confirm its specificity to cardiac fibroblasts and that it would not functionally impact cardiomyocytes in terms of systolic force. In this experiment, EHTs seeded with isolated NRVMs and NRCFs were incubated for eight days with either DMSO in the control (Ctrl) group, or with 10 μM SB-431542 in the SB group to match the duration of reverse remodeling before testing (Figure 4C). OCT scans showed no difference in tissue cross-sectional areas between the two groups following drug incubation (Figure 4D), but SB group tissues had the expected lowered stiffness profile compared with Ctrl tissues (Figure 4E, 2-way ANOVA $P < 0.0001$). Less stiff SB tissues also had marginal increase in slack length (Figure 4F, $P = 0.0464$). Looking at the active mechanics, the two groups did have very similar normalized peak forces at 1Hz pacing and 10% stretch (Figure 4G, $P = 0.5020$), but SB tissues demonstrated significantly faster twitch, resulting in shorter TTP (Figure 4H, $P < 0.0001$) and RT50 (Figure 4I, $P = 0.0002$) compared with Ctrl tissues. This meant that, from beat to beat, SB tissues spent less time in systole as shown by the force-time integral (Figure 4J, $P = 0.0058$). Moreover, knowing that collagen from cardiac fibroblasts played a dominant role in passive mechanics in longer stretch [31], linear correlations were performed between active mechanics and tissue stiffness at 10% stretch. Lack of correlation between normalized peak force and stiffness (Figure 4K, $P = 0.2632$) and similar normalized peak force between Ctrl and SB group confirmed that SB-431542 did not functionally affect cardiomyocytes. Additionally, the significant correlations between TTP and stiffness (Figure 4L, $P = 0.0218$) and RT50 and stiffness (Figure 4M, $P < 0.0001$) further validated that cardiac fibroblast activity was highly correlated with the duration of tissue contraction.

Collectively, SB-431542 altered passive mechanical profiles, which were significantly correlated with shortened active twitches. Meanwhile, it did not affect peak force production by cardiomyocytes. This parallels findings of at least one other group, that observed that

cardiomyocytes did not seem to respond to canonical TGF-β signaling blockade, and that TGF-β-neutralizing antibody therapy did not restore cardiomyocyte systolic dysfunction in pressure-overloaded mice hearts [32]. We concluded that SB-431542 constitutes a reasonably specific modulator of fibroblast activity in our EHTs.

Effects of sarcomeric myosin inhibition on the time-course of in-vitro reverse remodeling

Having established the time constant of reverse remodeling and role of fibroblast activity in our system, we next examined the role of active sarcomeric contraction in reverse remodeling. To this end, we allowed EHTs that had been stretched to 20% (as before) to remodel either in the presence or absence of continued 500 nM mavacamten exposure (SIRR, sarcomere-inhibited reverse remodeling, and RR, reverse remodeling, respectively). Control groups were also included in which tissues were not subjected to the stretch protocol, either with mavacamten during the nine-day recovery period (DC, drug control) or without (Ctrl). Finally, data were collected at two time points, at either day 1 or day 9 post unloading (Timepoints 1 and 2, respectively). This gave a total of 8 groups (Figure 5A, all groups $n \geq 6$ from four batches of tissues). Mavacamten was washed out for 30 min prior to data collection during mechanical testing.

Representative normalized passive stress traces showed visible separations in passive properties among the groups (Figure 5B). Most notably, the RR2 group was able to reverse remodel back to a passive mechanical profile similar to Ctrl2, while the SIRR2 group at the same time point was less stiff, being unable to regain control levels of passive stiffness. 3-way ANOVA analysis of the slack length indicated statistically significant interactions among the groups, meaning that mavacamten treatment was a significant modulator of reverse remodeling in both degree and time course (Figure 5C, $P = 0.0116$). The significant difference between RR2 and SIRR2 demonstrated attenuation of reverse remodeling in the absence of active contraction ($P = 0.0168$, effect size = 1.5). Interestingly, administration of mavacamten to unstretched tissue did not alter slack length, suggesting that the connection between tissue slack length and sarcomeric contraction is specifically relevant to the remodeling scenario, and not normal tissue maintenance (compare DC2 and Ctrl2 in Figure 5C).

In order to have a more detailed understanding of the passive mechanical behavior, we compared the stiffness of the EHTs at 7% stretch (Figure 5D). 3-way ANOVA analysis of the stiffness at 7% stretch indicated significant interaction among the groups, meaning that stretch and mavacamten treatment significantly altered the time-course of remodeling. These experiments revealed a striking increase in stiffness in the RR group during the 9 days after unloading (RR1 vs. RR2, $P < 0.0001$, effect size = 1.6), and suggested a stretch-induced role for activated cardiac fibroblasts in re-stiffening the matrix. The far greater stiffness in RR2 tissues compared with control (Ctrl2) further implicated the role of active fibroblasts ($P = 0.0438$, effect size = 0.6). Moreover, the significant difference between RR2 and SIRR2 in both slack length (Figure 5D, $P = 0.0168$) and stiffness (Figure 5E, $P = 0.0306$) revealed that contractile activity played a role in augmenting the reverse remodeling on top of the fibroblast-based ECM and diastolic force recovery. Furthermore, length-dependent activation of EHTs were compared in the Frank-Starling gain at 1Hz pacing and up to 10% stretch (Figure 5E). The marked recovery of Frank-Starling gain from RR1 to RR2 demonstrated the presence of reverse remodeling (duration of reverse remodeling $P = 0.014$) and the role of cardiomyocyte contractility in the recovery process (mavacamten $P = 0.0002$). It was also noted that the robust length-dependent activation of Ctrl2 tissues offered indirect evidence of mature sarcomeres in our EHTs.

Representative active twitch contraction data from select groups were plotted together (Figure 5F) and showed clear recovery in the active force from RR1 to RR2. A closer look at the normalized peak forces of each group at 1Hz pacing (Figure 5G) showed the same trend, with RR2 able to reverse back to the same level as Ctrl2. There was also significant interaction in time to peak force among the groups (Figure 5H, $P = 0.0002$), with RR2 having slower time to peak than RR1 and Ctrl2. Collectively, this experiment hinted at the potential roles of both cardiomyocytes and fibroblasts to achieve an advanced degree of reverse remodeling.

Evidence for cardiomyocyte-fibroblast interaction in reverse remodeling

After observing the separate contributions of both active sarcomeric contraction and activated fibroblasts on reverse remodeling, we next examined the interaction of these two factors. In this experiment, EHTs were subjected to the stretch/unloading protocol as before, then

treated during reverse remodeling with either 0.5 μM mavacamten (sarcomere-inhibited reverse remodeling group, SIRR), 10 μM SB-431542 (fibroblast-inhibited reverse remodeling group, FIRR), or a combination of both (double-inhibited reverse remodeling group, DIRR). After conditioning, the tissues were characterized to identify possible interaction (Figure 6A). Both drugs were washed out for 24 hours before mechanical testing. All data came from EHTs in a single batch.

Representative stretch traces for all four groups showed different passive mechanical profiles. Clear separations were observed among the groups, especially between RR and the other three groups (Figure 6B). To ascertain whether the magnitude of reverse remodeling was statistically different among the groups, a 3-way ANOVA analysis with repeated measures was conducted for the passive stresses (Figure 6C). Significant interaction was found among the three factors (mavacamten treatment, SB-43152 treatment, and tissue stretch, 3-way ANOVA $P = 0.0151$). This indicated that sarcomere contraction and fibroblast activity interacted synergistically to produce diastolic reverse remodeling. Full remodeling was only evident across all levels of tissue stretch when both cardiomyocytes and cardiac fibroblasts were uninhibited. Analysis of passive stress at culture length also showed significant interactions from the 3-way ANOVA analysis (Figure 6D, $P = 0.0013$), with RR recovering the most diastolic stress compared to the rest of the three groups (effective sizes > 2.2). This further confirmed the synergistic role of both cell types.

Without the active cardiomyocytes, the activated fibroblasts alone simply stiffened the tissues without completely taking up the slack introduced by the stretch protocol (Figure 6E). Having established that RR regained similar slack length to Ctrl at the same time point (RR2 vs. Ctrl2, Figure 5C), the higher slack length of SIRR compared with RR (Figure 6E) indicates an incomplete recovery ($P < 0.0001$, effect size = 2.2). Two-way ANOVA analysis of stiffness at 95% culture length indicated significant interaction among the four groups (Figure 6F, $P = 0.0011$) and confirmed the lack of reverse modeling without sarcomere contraction for SIRR, without fibroblast activity for FIRR, or both at low stretch compared with RR with the highest stiffness of all groups (2-way ANOVA $P < 0.0001$, effect size = 2). Moreover, two-way ANOVA analysis of stiffness at 9% stretch found that only SB-431542 had a significant P value (Figure 6G, $P < 0.0001$), suggesting that diastolic reverse remodeling required significant

cardiomyocyte-fibroblast interaction at strains near culture length but was dominated by fibroblast activity at higher strains.

Active mechanics demonstrated additional cardiomyocyte-fibroblast functional interactions. Representative twitches were plotted at 1Hz pacing and showed marked recovery for RR (Figure 6H). RR tended to recover normalized peak contraction force better than the treated groups (Figure 6I, effect sizes > 0.7), but this did not reach statistical significance (2-way ANOVA P = 0.0795). However, significant interactions were found for the twitch kinetic parameters time to peak (TTP, Figure 6J, 2-way ANOVA P = 0.01, effect sizes > 2.3) and the relaxation to 50% from the peak force (RT50, Figure 6K, 2-way ANOVA P = 0.0003, effect sizes > 2.1). In both cases, RR tissues produced the slowest TTP and RT50. Moreover, force-time integral offered a look at the time tissues spent in systole on a beat-to-beat basis, and again showed that only RR tissues were able to recover to Ctrl-level force-time integral value (Figure 6L).

Active twitch properties are correlated with matrix stiffness

In order to understand whether altered twitch properties in the RR group were dependent on tissue remodeling, we performed linear regression of normalized peak force, TTP, and RT50 vs stiffness for individual EHTs across all treatment groups (Figure 7A-C). All three twitch properties were significantly correlated with tissue stiffness. Stiffening of EHTs appeared to result in larger, slower twitches with a more prominent effect on tissue relaxation. This collectively indicated that the increase in matrix stiffness provoked by the stretch protocol profoundly affected EHT active mechanics, both in kinetics and in magnitude of the contraction. At the same exposure time and magnification, polarized light microscopy images of tissues stained with picrosirius red from all four groups were indicative of enhanced total collagen content in RR EHTs compared with the other groups (Figure 7D-G).

Evidence of reverse remodeling is observed in human EHT platform

To further validate our *in vitro* reverse remodeling model, the reverse remodeling experiments were performed in human EHT model with human induced pluripotent stem cell-derived cardiomyocytes (hiPSC-CMs) and adult cardiac fibroblasts (HCFs) (Figure 8A). One million cells were seeded per tissue with 80% hiPSC-CMs and 20% HCFs, and biomechanical

testing was conducted immediately after unloading (timepoint 1) and 9 days after unloading (timepoint 2). After stretch, RR1 group had significantly reduced tissue stiffness (Figure 8B) but RR2 would recover stiffness after 9 days compared to the Ctrl2 (Figure 8C). Compared to Ctrl1, RR1 also experienced significantly increased slack length (Figure 8D), markedly lowered peak stress (Figure 8E, F), slightly elevated TTP (Figure 8G), the same RT50, and significantly depressed Frank-Starling response to stretch (Figure 8I). However, after 9 days of reverse remodeling, RR2 showed comparable slack length to Ctrl2 (Figure 8J) and peak force and stress (Figure 8K, L). Reduced TTP and identical RT50 were also observed (Figure 8M, N). Lastly, Frank-Starling response of RR2 recovered in lower stretch range but still showed significant deviation at higher stretch percentage (Figure 8O).

Omecamtiv mecarbil improves reverse remodeling in human EHTs

To further test the hypothesis that active contraction contributes to the reverse remodeling process, cardiac specific inotrope omecamtiv mecarbil was used in a group of stretch and unloaded tissues (group name OM) to augment its contractility after unloading [33]. Biomechanical testing was performed 9 days post-unloading and results were compared to the reverse remodeling group without the drug serving as the new control (Ctrl group, Figure 9A). 9 days after unloading, similar tissue stiffness profiles between Ctrl and OM groups were observed (Figure 9B), and a marginally improved slack length result was seen for OM tissues (Figure 9C). In addition, the OM group demonstrated significantly increased peak stress (Figure 9D, E) while maintaining near-identical active kinetics in TTP and RT50 after 24-hr drug washout (Figure 9F, G). Lastly, OM tissues revealed marked improvement in Frank-Starling response over the Ctrl group (Figure 9H). Collectively, OM-treated tissues showed enhanced reverse remodeling results in both passive and active mechanics compared to untreated reverse remodeling controls.

Discussion

To our knowledge, this study is the first of its kind to specifically characterize the interaction of cardiomyocytes and cardiac fibroblasts in a simple in vitro representation of myocardial reverse remodeling. A series of controlled in vitro experiments in an engineered three-dimensional tissue model revealed an essential role for both cell types in successful recovery of both active and passive tissue functions.

Reflecting on these results, we propose a mechanistic model for the processes that drive reverse remodeling (Figure 10). In this ratchet-and-gear model, cardiac fibroblasts act as a ratchet, holding in place the temporary gains made by the cyclically contracting cardiomyocytes (gear). When fibroblast activity is curtailed, as when a TGF-β inhibitor is used, cyclical contractions of cardiomyocytes are insufficient to remove slack from the tissue (Figure 10A). When cardiomyocyte activity is inhibited as in the case of mavacamten incubation, fibroblasts alone can only lock the ratchet and stiffen the system in place, resulting in incomplete recovery of tissue shape (Figure 10B). Full recovery of passive and active myocardial properties following chronic stretch only occurs when both fibroblasts and cardiomyocytes are fully engaged (Figure 10A). This paradigm is further supported by our observations of enhanced remodeling after treatment with OM, which enhances sarcomeric contraction (Figure 9).

We choose mavacamten to modulate myofilament-based contraction in our *in vitro* model for several reasons. First, mavacamten targets cardiac myosin isoforms specifically and does not affect fast skeletal or non-muscle isoforms [34,35]. Moreover, mavacamten was developed to reduce peak tension without affecting calcium transients [34]. Based on this, we used the drug to prevent possible tissue injury during the static stretch phase. We also chose to use omecamtiv mecarbil as a target approach to enhance cardiac myosin ATPase activity without perturbing calcium cycling or other myosins [33]. Second, extended mavacamten use after unloading (Figures 5, 6) served to test the hypothesis that active contraction contributes to the recovery process. Since mavacamten does not affect calcium homeostasis, we focused on the improvement of diastolic and systolic mechanical properties as measures of reverse remodeling. In addition, we looked into the role of activated cardiac fibroblasts that sense and respond to

reduced cardiomyocyte stiffness [36].

Although fibroblast activity may be generally viewed as pathogenic in heart failure, our experiments suggest that these cells play an essential role in recovery after unloading. Matrix metalloproteinases (MMPs), which denature and degrade collagen, are shown to be downregulated after unloading, protecting ECM from further damage [37]. At the same time, tissue inhibitors of metalloproteinases (TIMPs) are upregulated after unloading [38]. However, studies disagree on the ultimate consequence of MMP/TIMP expression changes. Decreased collagen content and fibrosis have been reported after LVAD implantation [39–43], while other studies show an increase in collagen content and the ratio of collagen type I to III with LVAD support [37,44–46]. Such apparently contradictory findings may simply reflect a biphasic fibroblast response to unloading. This is supported by at least one study, which showed an increase in collagen synthesis and the ratio of type I to III collagen up to 200 days after LVAD implantation and a decrease thereafter [46].

Our *in-vitro* reverse remodeling EHT model seems to recapitulate the initial pro-fibrotic phase of ECM changes after unloading. Responding to the mechanical unloading, tissues allowed to have undisturbed recovery in RR groups from both experiments show significantly increased stiffness compared with other unloaded groups (Figure 5D, 6F, 6G). At the same time, there is noticeable recovery in peak stress (Figure 5G and 6I) accompanied by a decrease in active contraction speed in terms of both TTP (Figure 5H, 6J) and RT50 (Figure 6K). This is consistent with a previous report that increased collagen heavily contributes to an increase in systolic force and slower active twitch kinetics [24]. Our findings may help explain why LVAD patients with acute HF are more likely to have greater cardiac function recovery. Specifically, it seems that when the onset of fibroblast activation is synchronous with unloading, it may help normalize diastolic and systolic dysfunction through fibroblast-cardiomyocyte interactions.

Our in vitro system mimics aspects of cardiomyocyte recovery reported in LVAD patients after unloading, which can include remarked drop in plasma BNP level [47,48], reversal of contractile dysfunction, and improvement of calcium handling and cytoskeletal protein structures [46,49–52]. However, there is debate on the possible detriment of prolonged unloading on the cardiomyocytes. Studies of explanted patient tissue suggest that cardiomyocyte atrophy and

degeneration do not occur with long-term LVAD support [9,53], while studies of unloaded myocardium in rat show reduced contractility and myofilament sensitivity to calcium [54,55].

To address the possibility of atrophy during unloading, several pharmacological treatments have been used in combination with LVADs to facilitate reverse remodeling. These include administration of the β_2-adrenergeic receptor agonist clenbuterol as part of the Harefield protocol along with a β_1-blocker [56–58] and have led to some promising results [58,59]. However, therapies inspired by Harefield protocols fail to prevent myocardial atrophy and cause downregulation of β_2-adrenergeic receptor with chronic clenbuterol administration [60], result in less improvement in EC-coupling as a combination therapy of β_2-agonist and β_1-blocker than using either β_2-agonist or β_1-antagonist alone [58], and do not demonstrate a synergistic effect of β_2-agonist and β_1-blocker in ischemic HF models [61]. In light of the studies reported here, it seems possible that a lack of proper fibroblast activity could be the missing component from the Harefield-type protocols.

Lastly, although the goal of this study is to use our *in vitro* model to gain a better fundamental understanding of the reverse remodeling phenomenon with a reductionist approach, it should be acknowledged that our current method does not precisely capture the in vivo conditions. First, dynamic control of EHT loading conditions would be required to begin to recapitulate the hemodynamic effects of LVAD implantation. Future work could include applying our recently reported bioreactor to imitate *in vivo* work loops on human EHTs, enabling greater physiological fidelity in our model [62]. In addition, our *in vitro* model does not specifically include all of the complex factors present in chronic heart failure, including changes to neurohumoral activation, excitation-contraction coupling, apoptotic and metabolic signaling, cardiomyocyte size and shape, or fetal gene programming [41,63]. Lastly, given the focused nature of our study, we have not distinguished between *in vivo* myocardial recovery and myocardial remission [64]. The conclusions from this study are limited to the mechanisms of cellular contraction that may be required to accomplish bulk myocardial morphology changes. Determining the extent to which our findings are applicable to reverse myocardial remodeling in a clinical setting will require future study.

Acknowledgements

We thank Mahammad Camara for his work on an early prototype of the EHT stretch device.

Sources of Funding

This work was supported by a National Science Foundation CAREER Award (1653160) and NIH 1R01HL136590 (both to S.G.C). L.R.S was supported by a Paul and Daisy Soros Fellowship for New Americans, an American Heart Association Predoctoral Fellowship, and a NIH/NIGMS Medical Scientist Training Program Grant (T32GM007205).

Disclosures

S.G.C. holds equity ownership in Propria LLC, which has licensed technology used in the research reported in this publication. L.R.S. and S.S. declare no conflicts of interest.

Data availability statement

The raw/processed data required to reproduce these findings cannot be shared at this time due to technical or time limitations.

References

[1] E.A. Rose, A.C. Gelijns, A.J. Moskowitz, D.F. Heitjan, L.W. Stevenson, W. Dembitsky, et al. Randomized Evaluation of Mechanical Assistance for the Treatment of Congestive Heart Failure (REMATCH) Study Group, Long-Term Use of a Left Ventricular Assist Device for End-Stage Heart Failure. N. Engl. J. Med. 2001; 345: 1435–1443.

[2] L.W. Miller, F.D. Pagani, S.D. Russell, R. John, A.J. Boyle, K.D. Aaronson, et al. Use of a continuous-flow device in patients awaiting heart transplantation N. Engl. J. Med. 2007; 357: 885–896.

[3] F.D. Pagani, L.W. Miller, S.D. Russell, K.D. Aaronson, R. John, A.J. Boyle, et al. Extended Mechanical Circulatory Support with a Continuous-Flow Rotary Left Ventricular Assist Device. J. Am. Coll. Cardiol. 2009; 54: 312–321.

[4] M.S. Slaughter, J.G. Rogers, C.A. Milano, S.D. Russell, J. V. Conte, D. Feldman, et al. Advanced Heart Failure Treated with Continuous-Flow Left Ventricular Assist Device. N. Engl. J. Med. 2009; 361: 2241–2251.

[5] A. Tsiouris, Short and long term outcomes of 200 patients supported by continuous-flow left ventricular assist devices. World J. Cardiol. 2015; 7: 792.

[6] E.J. Benjamin, M.J. Blaha, S.E. Chiuve, M. Cushman, S.R. Das, R. Deo, et al. Heart Disease and

Stroke Statistics'2017 Update: A Report from the American Heart Association. Circulation. 2017; 135: e146–e603.

[7] S. Maybaum, D. Mancini, S. Xydas, R.C. Starling, K. Aaronson, F.D. Pagani, et al. Cardiac improvement during mechanical circulatory support: A prospective multicenter study of the LVAD working group. Circulation. 2007; 115: 2497–2505.

[8] S. Maybaum, G. Kamalakannan, S. Murthy. Cardiac Recovery During Mechanical Assist Device Support. YSTCS. 2008; 20: 234–246.

[9] K. Muthiah, D.T. Humphreys, D. Robson, K. Dhital, P. Spratt, P. Jansz, et al. Longitudinal structural, functional, and cellular myocardial alterations with chronic centrifugal continuous-flow left ventricular assist device support. J. Hear. Lung Transplant. 2017; 36: 722–731.

[10] S. Miyagawa, Koichi Toda, T. Nakamura, Y. Yoshikawa, Satsuki Fukushima, S. Saito, et al. Building a bridge to recovery: the pathophysiology of LVAD-induced reverse modeling in heart failure. Surg Today. 2016; 3: 149–154.

[11] D.G. Jakovljevic, M.H. Yacoub, S. Schueler, G.A. MacGowan, L. Velicki, P.M. Seferovic, et al. Left Ventricular Assist Device as a Bridge to Recovery for Patients with Advanced Heart Failure. J. Am. Coll. Cardiol. 2017; 69: 1924–1933.

[12] M.C. Deng, L.B. Edwards, M.I. Hertz, A.W. Rowe, B.M. Keck, R. Kormos, et al. Mechanical circulatory support device database of the international society for heart and lung transplantation: Second annual report – 2004. J. Hear. Lung Transplant. 2004; 23: 1027–1034.

[13] D.J. Goldstein, S. Maybaum, T.E. MacGillivray, S.A. Moore, R. Bogaev, D.J. Farrar, et al. Young patients with nonischemic cardiomyopathy have higher likelihood of left ventricular recovery during left ventricular assist device support. J. Card. Fail. 2012; 12: 392–395.

[14] D.M. Mancini, A. Beniaminovitz, H. Levin, K. Catanese, M. Flannery, M. DiTullio, et al. Low Incidence of Myocardial Recovery After Left Ventricular Assist Device Implantation in Patients with Chronic Heart Failure. Circulation. 1998; 98: 2383–2389.

[15] O.H. Frazier, A.C.W. Baldwin, Z.T. Demirozu, A.M. Segura, R. Hernandez, H. Taegtmeyer, et al. Ventricular reconditioning and pump explantation in patients supported by continuous-flow left ventricular assist devices. J. Hear. Lung Transplant. 2015; 34: 766-772.

[16] A.M. Segura, L. Dris, E.K. Massin, F.J. Clubb, L.M. Buja, O.H. Frazier, et al. Heart failure in remission for more than 13 years after removal of a left ventricular assist device., Tex. Heart Inst. J. 2014; 41: 389–94.

[17] M.S. Sharma, S.A. Webber, V.O. Morell, S.K. Gandhi, P.D. Wearden, J.R. Buchanan, et al. Ventricular Assist Device Support in Children and Adolescents as a Bridge to Heart Transplantation. Ann Thorac Surg. 2006; 82: 926-932.

[18] R. Hetzer, M. Francisco Del Maria Javier, E. Maria, D. Walter. Role of paediatric assist device in bridge to transplant. Ann Cardiothorac Surg. 2018; 7: 82–98.

[19] X.X. Miera, X. Xmd, X. Germannd, X. Xmy, Y. Chod, X. Photiadis, et al. Bridge to recovery in children on ventricular assist devices-protocol, predictors of recovery, and long-term follow-up. J. Hear. Lung Transplant. 2018; 37: 1459–1466.

[20] J. Kasten, D. Rakheja, S. Zhang, P. Thankavel, B.B. Das. Reverse histologic remodeling after mechanical unloading of failing hearts in children with dilated cardiomyopathy. J. Hear. Lung Transplant. 36 (2017) 1268–1271.

[21] D. Grundy. Principles and standards for reporting animal experiments in The Journal of Physiology and Experimental Physiology. J. Physiol. 2015; 593: 2547–2549.

[22] J. Schwan, A.T. Kwaczala, T.J. Ryan, O. Bartulos, Y. Ren, L.R. Sewanan, et al. Anisotropic engineered heart tissue made from laser-cut decellularized myocardium. Sci. Rep. 2016; 6: 32068.

[23] X. Lian, J. Zhang, S.M. Azarin, K. Zhu, L.B. Hazeltine, X. Bao, et al. Directed cardiomyocyte differentiation from human pluripotent stem cells by modulating Wnt/β-catenin signaling under fully defined conditions. Nat. Protoc. 2013; 8:162–175.

[24] L.R. Sewanan, J. Schwan, J. Kluger, J. Park, D.L. Jacoby, Y. Qyang, et al. Extracellular Matrix from Hypertrophic Myocardium Provokes Impaired Twitch Dynamics in Healthy Cardiomyocytes. JACC Basic to Transl. Sci. 2019; 4: 495–505.

[25] R.H. Pires, N. Shree, E. Manu, E. Guzniczak, O. Otto. Cardiomyocyte mechanodynamics under conditions of actin remodeling. Philos. Trans. R. Soc. B Biol. Sci. 2019; 374: 20190081.

[26] J.G. Jacot, J.C. Martin, D.L. Hunt. Mechanobiology of cardiomyocyte development. J. Biomech. 2010; 43: 93–98.

[27] Y. Yang, H.J. Kim, K.-J. Woo, D. Cho, et al. Lipo-PGE1 suppresses collagen production in human dermal fibroblasts via the ERK/Ets-1 signaling pathway. PLoS One. 2017; 12: e0179614.

[28] F. Sader, J.F. Denis, H. Laref, S. Roy. Epithelial to mesenchymal transition is mediated by both TGF-β canonical and non-canonical signaling during axolotl limb regeneration. Sci. Rep. 9 (2019). https://doi.org/10.1038/s41598-018-38171-5.

[29] N.P. Dufton, C.R. Peghaire, L. Osuna-Almagro, C. Raimondi, V. Kalna, A. Chuahan, et al. Dynamic regulation of canonical TGFβ signalling by endothelial transcription factor ERG protects from liver fibrogenesis. Nat. Commun. 2017; 8: 1–14.

[30] J. Kim, J. Kim, S.H. Lee, S. V. Kepreotis, J. Yoo, J.S. Chun, et al. Cytokine-like 1 regulates cardiac fibrosis via modulation of TGF-β Signaling. PLoS One. 2016; 11: e0166480.

[31] H.L. Granzier, T.C. Irving, Passive Tension in Cardiac Muscle: Contribution of Collagen, Titin, Microtubules, and Intermediate Filaments. Biophys J. 1995; 68: 1027-1044.

[32] N. Koitabashi, T. Danner, A.L. Zaiman, Y.M. Pinto, J. Rowell, J. Mankowski, et al. Pivotal role of cardiomyocyte TGF-β signaling in the murine pathological response to sustained pressure overload, J. Clin. Invest. 2011; 121: 2301–2312.

[33] F.I. Malik, J.J. Hartman, K.A. Elias, B.P. Morgan, H. Rodriguez, K. Brejc, et al. Cardiac myosin

activation: A potential therapeutic approach for systolic heart failure. Science. 2011; 331: 1439–1443.

[34] E.M. Green, H. Wakimoto, R.L. Anderson, M.J. Evanchik, J.M. Gorham, B.C. Harrison, et al. A small-molecule inhibitor of sarcomere contractility suppresses hypertrophic cardiomyopathy in mice. Science. 2016; 351: 617–621.

[35] B. Scellini, N. Piroddi, M. Dente, G. Vitale, J.M. Pioner, R. Coppini, et al. Mavacamten has a differential impact on force generation in myofibrils from rabbit psoas and human cardiac muscle. J. Gen. Physiol. 2021; 153: e202012789.

[36] P.A. Galie, M. V. Westfall, J.P. Stegemann. Reduced serum content and increased matrix stiffness promote the cardiac myofibroblast transition in 3D collagen matrices, Cardiovasc. Pathol. 2011; 20: 325–333.

[37] S. Klotz, R.F. Foronjy, M.L. Dickstein, A. Gu, I.M. Garrelds, A H Jan Danser, et al. Mechanical Unloading During Left Ventricular Assist Device Support Increases Left Ventricular Collagen Cross-Linking and Myocardial Stiffness. Circulation. 2005; 112: 364-374.

[38] Y.Y. Li, Y. Feng, C.F. Mctiernan, W. Pei, C.S. Moravec, P. Wang, et al. Downregulation of Matrix Metalloproteinases and Reduction in Collagen Damage in the Failing Human Heart After Support with Left Ventricular Assist Devices. Circulation. 2001; 104: 1147-1152.

[39] S. Taketani, Y. Sawa, N. Fukushima, T. Masai, N. Kawaguchi, S. Onishi, et al. Myocardial histological changes in dilated cardiomyopathy during a long-term left ventricular assist device support. Heart Vessels. 1997; 12: 98–100.

[40] J. Müller, G. Wallukat, Y.G. Weng, M. Dandel, S. Spiegelsberger, S. Semrau, et al. Weaning from mechanical cardiac support in patients with idiopathic dilated cardiomyopathy. Circulation. 1997; 96: 542–549.

[41] S. Xydas, R.S. Rosen, C. Ng, M. Mercando, J. Cohen, M. DiTullio, et al. Mechanical unloading leads to echocardiographic, electrocardiographic, neurohormonal, and histologic recovery. J. Hear. Lung Transplant. 2006; 25: 7–15.

[42] B.A. Bruckner, S.J. Stetson, A. Perez-Verdia, K.A. Youker, B. Radovancevic, J.H. Connelly, et al. Regression of fibrosis and hypertrophy in failing myocardium following mechanical circulatory support, J. Hear. Lung Transplant. 2001; 20: 457–464.

[43] J.D. Madigan, A. Barbone, A.F. Choudhri, D.L. Morales, B. Cai, M.C. Oz, et al. Time course of reverse remodeling of the left ventricle during support with a left ventricular assist device. J. Thorac. Cardiovasc. Surg. 2001; 121: 902–8.

[44] L.O. Thompson, C.A. Skrabal, M. Loebe, J.A. Lafuente, R.R. Roberts, A. Akgul, et al. Plasma neurohormone levels correlate with left ventricular functional and morphological improvement in LVAD patients. J. Surg. Res. 2005; 123: 25–32.

[45] W. Oriyanhan, H. Tsuneyoshi, T. Nishina, S. Matsuoka, T. Ikeda, M. Komeda. Determination of Optimal Duration of Mechanical Unloading for Failing Hearts to Achieve Bridge to Recovery in a

Rat Heterotopic Heart Transplantation Model. J. Hear. Lung Transplant. 2007; 26: 16–23.

[46] A.H. Bruggink, M.F.M. van Oosterhout, N. de Jonge, B. Ivangh, J. van Kuik, R.H.A.M. Voorbij, et al. Reverse Remodeling of the Myocardial Extracellular Matrix After Prolonged Left Ventricular Assist Device Support Follows a Biphasic Pattern. J. Hear. Lung Transplant. 2006; 25: 1091–1098.

[47] B. Sareyyupoglu, B.A. Boilson, L.A. Durham, C.G.A. McGregor, R.C. Daly, M.M. Redfield, et al. B-Type natriuretic peptide levels and continuous-flow left ventricular assist devices. ASAIO J. 2010; 56: 527–531.

[48] A.H. Bruggink, N. De Jonge, M.F.M. Van Oosterhout, D.F. Van Wichen, E. De Koning, J.R. Lahpor, et al. Brain natriuretic peptide is produced both by cardiomyocytes and cells infiltrating the heart in patients with severe heart failure supported by a left ventricular assist device. J. Hear. Lung Transplant. 2006; 25: 174–180.

[49] P.M. Heerdt, J.W. Holmes, B. Cai, A. Barbone, J.D. Madigan, S. Reiken, et al. Chronic Unloading by Left Ventricular Assist Device Reverses Contractile Dysfunction and Alters Gene Expression in End-Stage Heart Failure. Circulation. 2000; 102; 2713–2719.

[50] L.A. Aquila, P.M. McCarthy, N.G. Smedira, J.B. Young, C.S. Moravec, Cytoskeletal structure and recovery in single human cardiac myocytes. J. Hear. Lung Transplant. 2004; 23: 954–963.

[51] M. Vatta, S.J. Stetson, A. Perez-Verdia, M.L. Entman, G.P. Noon, G. Torre-Amione, et al. Molecular remodeling of dystrophin in patients with end-stage cardiomyopathies and reversal in patients on assistance-device therapy. Lancet. 2002; 359: 936–41.

[52] E.J. Birks, J.L. Hall, P.J.R. Barton, S. Grindle, N. Latif, J.P. Hardy, et al. Gene profiling changes in cytoskeletal proteins during clinical recovery after left ventricular-assist device support, Circulation. 2005; 112: I57-64.

[53] N.A. Diakos, C.H. Selzman, F.B. Sachse, J. Stehlik, A.G. Kfoury, O. Wever-Pinzon, et al. Myocardial atrophy and chronic mechanical unloading of the failing human heart: Implications for cardiac assist device-induced myocardial recovery. J. Am. Coll. Cardiol. 2014; 64: 1602–1612.

[54] G.K.R. Soppa, J. Lee, M.A. Stagg, U. Siedlecka, S. Youssef, M.H. Yacoub, et al. Prolonged Mechanical Unloading Reduces Myofilament Sensitivity to Calcium and Sarcoplasmic Reticulum Calcium Uptake Leading to Contractile Dysfunction. J. Hear. Lung Transplant. 2008; 27: 882–889.

[55] K. Ito, M. Nakayama, F. Hasan, X. Yan, M.D. Schneider, B.H. Lorell. Contractile reserve and calcium regulation are depressed in myocytes from chronically unloaded hearts. Circulation. 2003l; 107: 1176–82.

[56] J.K.F. Hon, M.H. Yacoub. Bridge to recovery with the use of left ventricular assist device and clenbuterol. Ann. Thorac. Surg. 2003; 75: S36-41,

[57] M. Navaratnarajah, U. Siedlecka, M. Ibrahim, C. Van Doorn, G. Soppa, A. Gandhi, et al. Impact of Combined Clenbuterol and Metoprolol Therapy on Reverse Remodelling during Mechanical

Unloading. PLoS One. 2014; 30: e92909.

[58] E.J. Birks, P.D. Tansley, J. Hardy, R.S. George, C.T. Bowles, M. Burke, et al. Left ventricular assist device and drug therapy for the reversal of heart failure. N. Engl. J. Med. 2006; 355: 1873–1884.

[59] E.J. Birks, R.S. George, M. Hedger, T. Bahrami, P. Wilton, C.T. Bowles, et al. Reversal of severe heart failure with a continuous-flow left ventricular assist device and pharmacological therapy: A prospective study. Circulation. 2011; 123: 381–390.

[60] H. Tsuneyoshi, W. Oriyanhan, H. Kanemitsu, R. Shiina, T. Nishina, S. Matsuoka, et al. Does the β2-agonist clenbuterol help to maintain myocardial potential to recover during mechanical unloading? Circulation. 2005; 112: I51-56.

[61] S. Xydas, A.R. Kherani, J.S. Chang, S. Klotz, I. Hay, C.J. Mutrie, et al. β2-adrenergic stimulation attenuates left ventricular remodeling, decreases apoptosis, and improves calcium homeostasis in a rodent model of ischemic cardiomyopathy. J. Pharmacol. Exp. Ther. 2006; 317: 553–561.

[62] R. Ng, L.R. Sewanan, A.L. Brill, P. Stankey, X. Li, Y. Qyang, et al. Contractile work directly modulates mitochondrial protein levels in human engineered heart tissues. Am. J. Physiol. Heart. Circ. Physiol. 2020; 318: H1516–H1524.

[63] A. van der Pol, M.F. Hoes, R.A. de Boer, P. van der Meer. Cardiac foetal reprogramming: a tool to exploit novel treatment targets for the failing heart. J. Intern. Med. 2020; 288: 491–506.

[64] G.H. Kim, N. Uriel, D. Burkhoff. Reverse remodelling and myocardial recovery in heart failure. Nat. Rev. Cardiol. 2018; 15: 83–96.

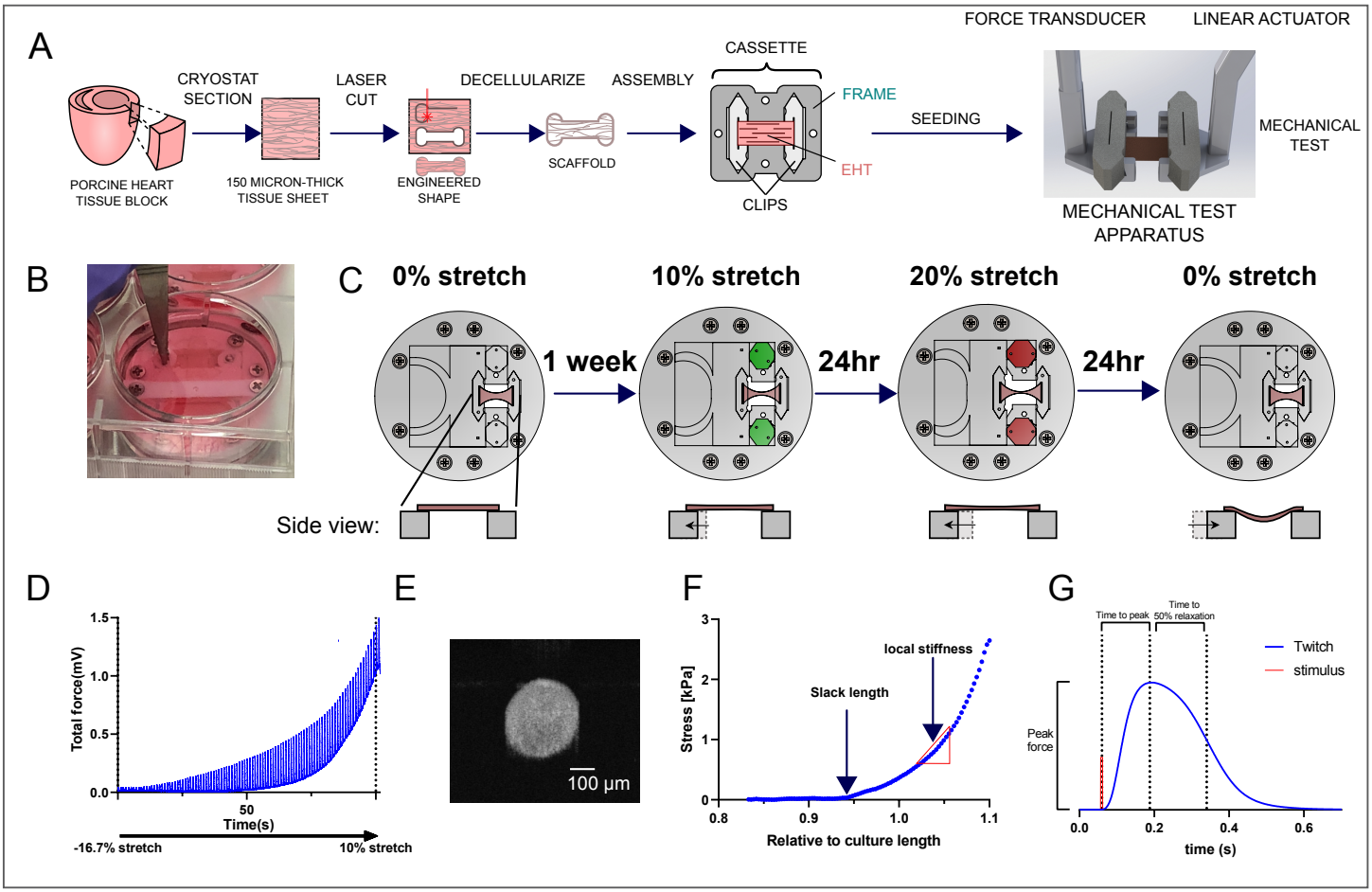

Figure 1. Engineered heart tissue (EHT) production, stretch, and data collection workflow.
A. schematics of engineered heart tissue (EHT) making process using decellularized porcine ventricular scaffold and isolated neonatal rat ventricular myocytes (NRVMs) and cardiac fibroblasts (NRCFs). EHTs were assembled at constant culture length and mechanically tested isometrically. **B**. An image of an EHT being stretched with our custom-made stretch device in a 6-well plate. **C**. Individual EHT static stretch protocol after 1 week of normal culture. The stretch was started at 10% stretch by turning the pair of octagons (highlighted in green), then increased to 20% for 24hr by further turning the octagons (highlighted in red), and ended with unloading. **D**. Representative raw data collected with our mechanical testing system. Data were collected with 2 kHz sampling rate and 1 Hz electrical stimulation while the tissue was being stretch. **E**. Representative tissue cross-sectional scan by optical coherence tomography. **F**. Processed and normalized representative passive stress profile was used to determine tissue slack length (the position where it started to develop passive force) and stiffness. **G**. Representative active twitch following a 1 Hz stimulus (in red). Automated scripts were used to measure peak force (PF), time to peak (TTP), time to 50% relaxation (RT50).

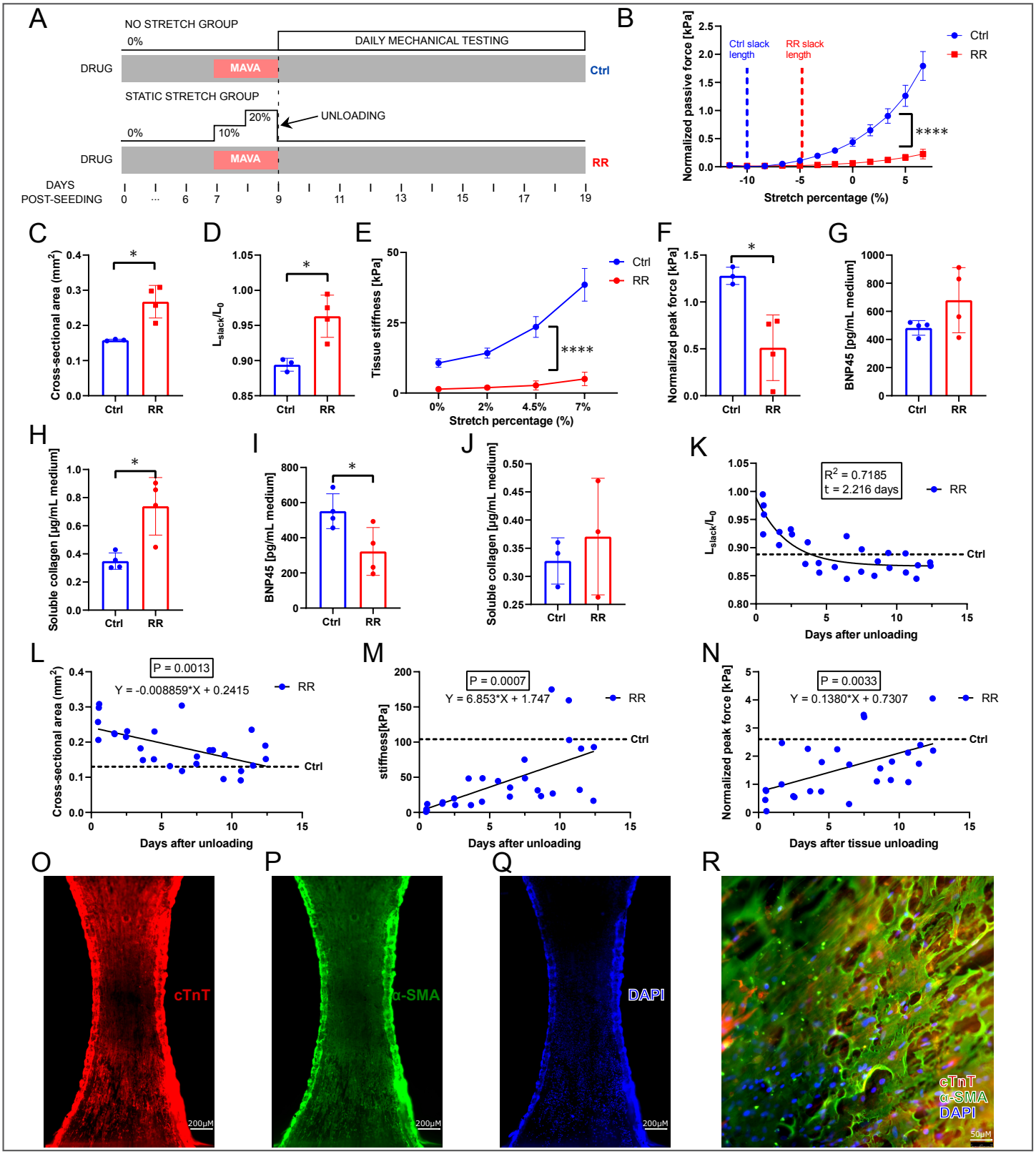

Figure 2. Reverse remodeling is observed and characterized in our in-vitro model following stretch and unloading.
A. Schematic of the experimental design. A control group (Ctrl) was compared to a reverse remodeling (RR) group with static step-wise stretch. Biomechanical testing was conducted immediately after unloading and every day for 12 days after unloading. Data in panels B-H were from tissues immediately after unloading (Ctrl tissue n = 3, RR n = 4). **B**. Normalized passive traces for both groups plotted over the majority of the stretch ($P < 0.0001$). **C**.Tissue cross-sectional areas obtained from OCT to normalize tissue passive force ($P = 0.0105$). **D**. Slack lengths were determined from tissues' passive stress profile (B) as a measure of mechanical deformation after stretch ($P = 0.0131$). **E**. Tissue stiffness was calculated from tissues' passive mechanical data with Matlab script ($P < 0.0001$). **F**. Normalized peak forces at 1Hz pacing and 10% stretch ($P = 0.0152$). **G**. BNP-45 level was measured by ELISA in cell culture medium after 48-hour stretch (n = 4). **H**. Newly synthesized collagen levels measured by soluble collagen assay in cell culture medium after 48-hour stretch ($P = 0.0106$, n = 4). **I**. BNP-45 level measured by ELISA in cell culture medium 24 hours after unloading ($P = 0.0344$, n = 4). **J**. Newly synthesized soluble collagen level in cell culture medium 9 days after unloading (n = 3). **K**. Time course study of tissue slack length up to 12 days after unloading to characterize the progression of reverse remodeling (n = 27). This was used to determine the data collection time points in subsequent experiments. Dashed line indicated the mean slack length value for unstretched control tissues at day 9 post-unloading as a reference. **L**. Time course study of tissue cross-sectional area up to 12 days after unloading. Dashed line indicates the mean value from the control group for reference. **M**. Time course study of tissue stiffness at 7% stretch from 0 to 12 days after unloading. Dashed line indicates the mean value from the control group for reference. **N**. Time course study of normalized peak force from 0 to 12 days after unloading. Dashed line indicates the mean value from the control group for reference. **O-Q**. Representative immunohistochemistry (IHC) tiled image of an RR tissue day 9 post-unloading stained for cardiac troponin T (cTnT, red), α-smooth muscle actin (α-SMA, green), and DAPI (blue). **R**. Representative IHC merged image of a RR tissue day 9 post-unloading stained for cTnT, α-SMA, and DAPI at 20x magnification. Experiments were analyzed with two-tailed unpaired t tests (C, D, F, G, H, I, J), 2-way ANOVA with repeated measures (B, E), non-linear regression (K), and linear regression (L, M, N). * $P < 0.05$, ** $P < 0.01$, *** $P < 0.001$, **** $P < 0.0001$. All error bars are expressed as standard deviations.

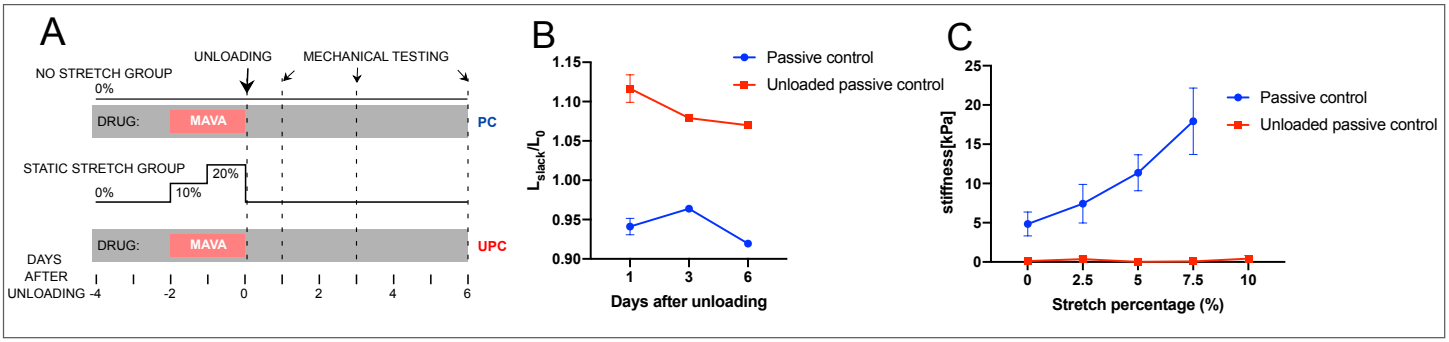

Figure 3. Decellularized tissue passive mechanics.
A. Passive control experimental design (n = 2). **B**. Slack lengths of the unstretched and stretch and unloaded decellularized tissues. **C**. Decellularized tissue stiffness at day 6 after unloading. All error bars are expressed as standard deviations.

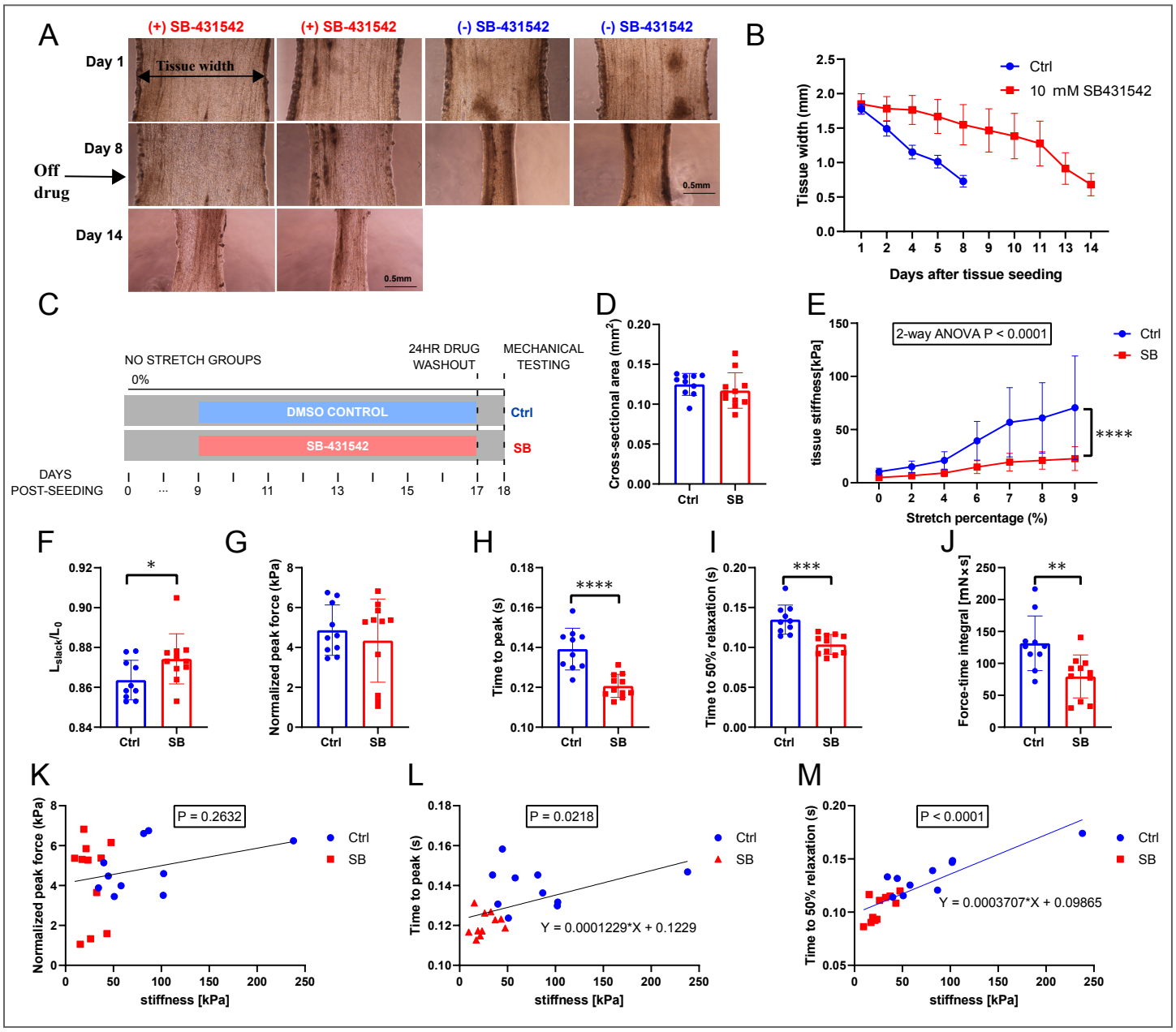

Figure 4. SB-431542 is an reversible TGF-beta inhibitor and functionally specific to cardiac fibroblasts in our EHT system.

A. Brightfield images of EHTs at 4x magnification. Tissues were seeded normally with isolated NRVMs and NRCFs, and one day after seeding, media were changed with or without 10 μM SB-431542. Media were changed every other day until day 8 when SB-431542 was removed to examine the reversibility of the drug. Control tissues did not show further width changes after day 8. **B**. Tissue width at the center of the tissues was quantified as a measure of the matrix remodeling and was plotted over time (n = 4 per group). **C**. SB-431542 control experiment design with DMSO vehicle as the control (Ctrl, n = 10) and 10μM SB-431542 as the experimental group (SB, n = 11) to examine the functional specificity of SB-431542 to cardiac fibroblasts. **D**. Cross-sectional areas of CTL and SB tissues. **E**. Tissue stiffness from culture length to 9% stretch ($P < 0.0001$). **F**. Slack lengths of CTL and SB tissues ($P = 0.0464$). **G**. Normalized peak forces at 1Hz pacing and 10% stretch ($P = 0.5020$). **H**. Time to peak (TTP) at 1Hz pacing and 10% stretch ($P < 0.0001$). **I**. Time to 50% relaxation (RT50) at 1Hz pacing and 10% stretch ($P = 0.0002$). **J**. Force-time integral at 1Hz pacing and 10% stretch ($P = 0.0058$). **K**. Non-significant correlation between normalized peak force and tissue stiffness at 10% stretch ($P = 0.2632$). **L**. Significant correlation between TTP and stiffness at 10% stretch ($P = 0.0216$). **M**. Significant correlation between RT50 and stiffness at 10% strtech ($P < 0.0001$). Two-tailed unpaired t tests (D, F, G, H, I, J), two-way ANOVA with repeated measures (E), and simple linear regressions (K-M) were performed. * $P < 0.05$, ** $P < 0.005$, *** $P < 0.001$, **** $P < 0.0001$. All error bars are expressed as standard deviations.

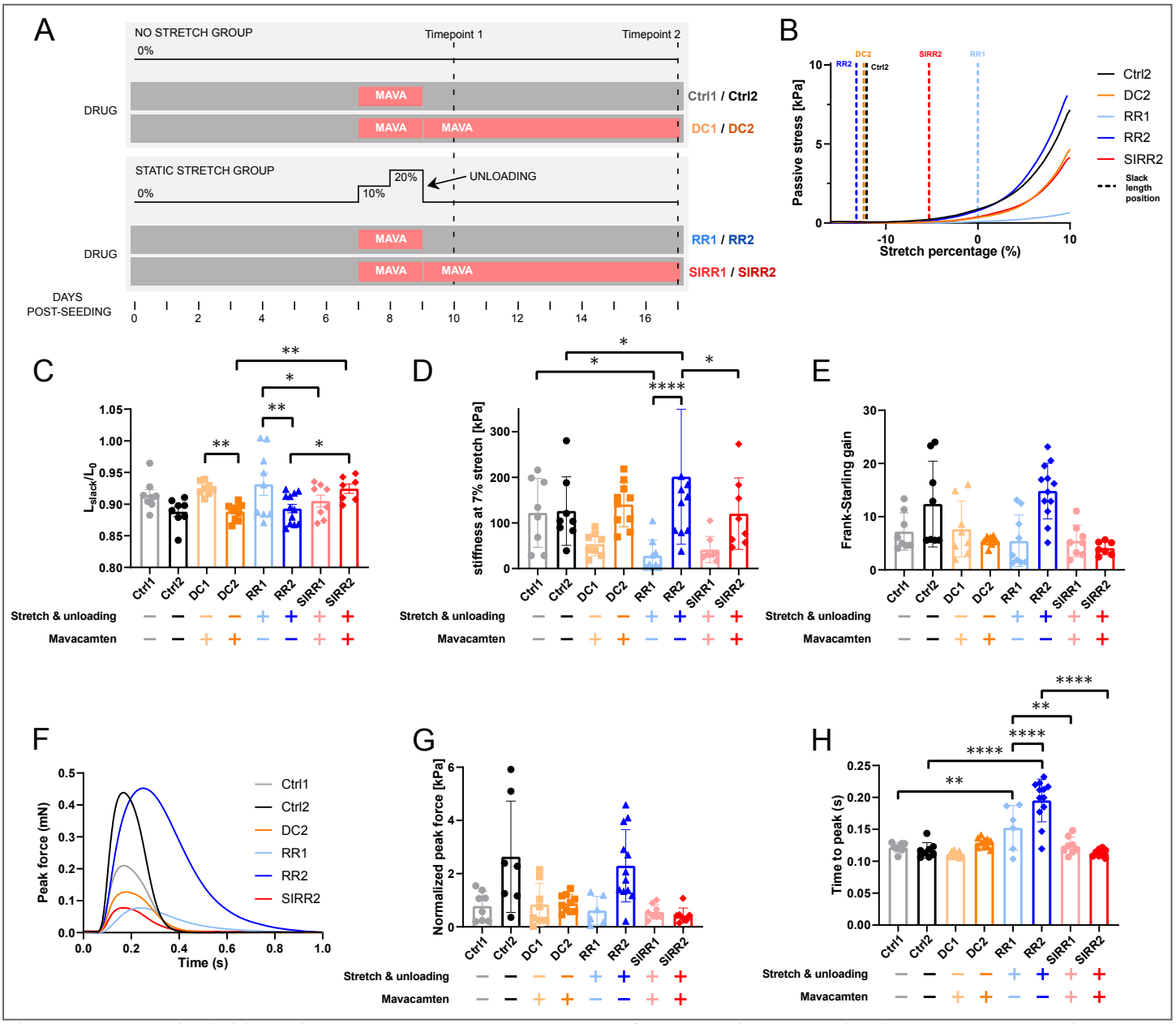

Figure 5. NRVM inhibition with mavacamten shows the role of sarcomeric contraction in reverse remodeling. **A**. 3-way ANOVA experimental design to assess the role of active contraction in reverse remodeling. The three factors were the stretch, mavacamten, and two data collection time points based on the time course study (Figure 2J). Ctrl1 n = 8, Ctrl2 n = 7, DC1 n = 8, DC2 n = 10, RR1 n = 6, RR2 n = 12, SIRR1 n = 8, SIRR2 n =7. **B**. Representative passive stress traces for select groups, with dashed lines indicating the slack length positions. **C**. Slack length (3-way ANOVA P = 0.0116). **D**. Tissue stiffness at 7% stretch (3-way ANOVA P = 0.0244). **E**. Frank-Starling gain at 1Hz pacing and up to 10% stretch (Duration of reverse remodeling P = 0.014, mavacamten P = 0.0002). **F**. Representative active twitch from select groups at 1Hz pacing and 10% stretch. **G**. Normalized peak forces of all groups at 1Hz pacing and 10% stretch. **H**. Time to peak of all groups at 1Hz pacing and 10% stretch (3-way ANOVA P = 0.0002). Experiments were analyzed with 3-way ANOVA analysis with planned comparisons (C, E, G, H). * P < 0.05, ** P < 0.01, *** P < 0.001, **** P < 0.0001. All error bars are expressed as standard deviations.

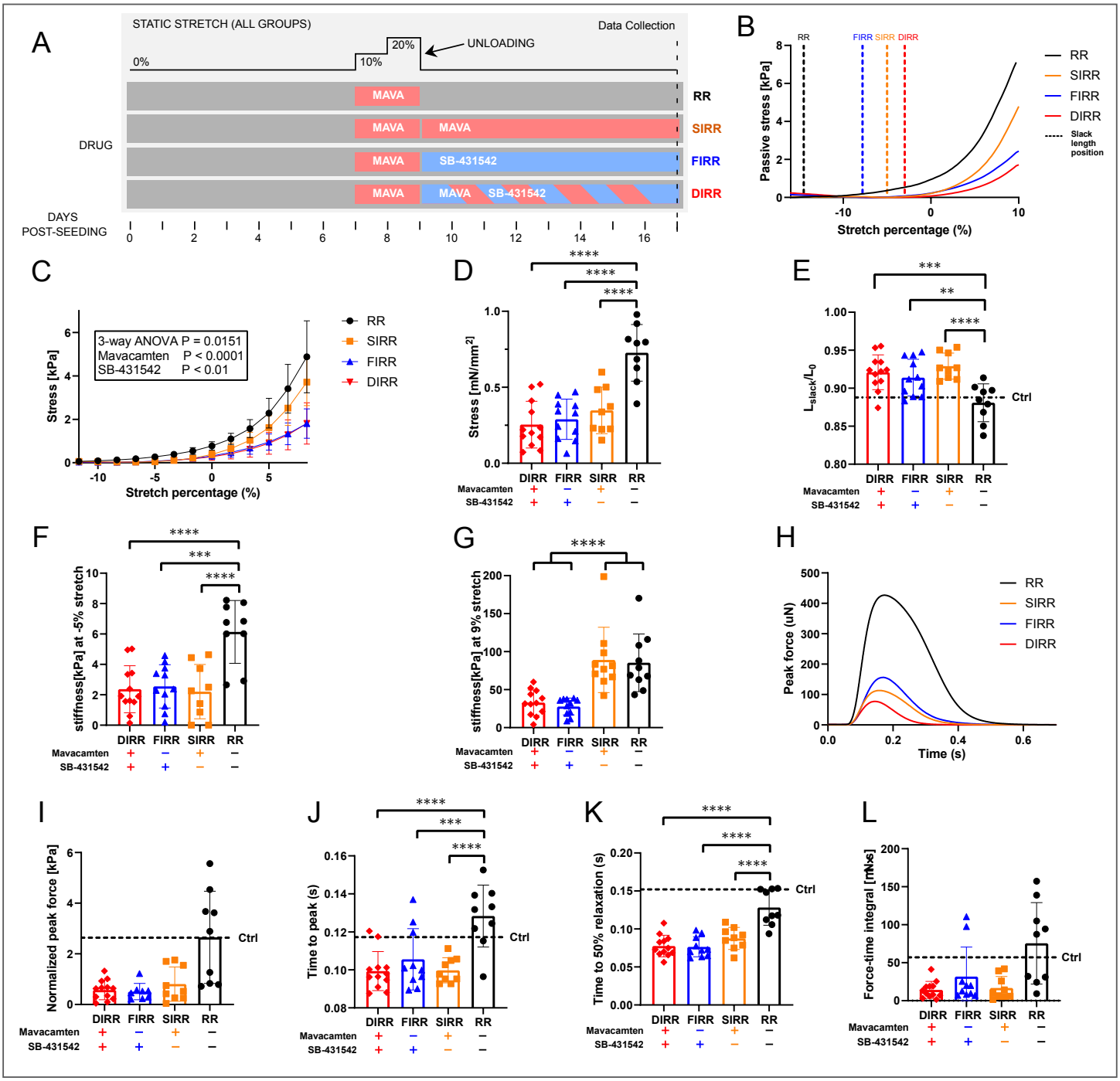

Figure 6. Interactions between NRVMs and NRCFs contribute to the reverse remodeling process.
A. Experimental design with RR group as the control. 500nM Mavacamten and 10μM SB-431542 were used to selectively inhibit myofilament activity and fibroblast activation. DIRR n = 12, FIRR n = 11, SIRR n = 9, RR n = 9. **B**. Representative stress traces normalized with tissue cross-sectional areas. Dashed lines indicated the slack length positions along the stretch. **C**. Force vs. length curves for all four groups (3-way ANOVA P = 0.0151). **D**. Passive stress comparisons at culture length (2-way ANOVA P = 0.0013). **E**. Slack length comparison (2-way ANOVA P = 0.0051) with dashed line indicating slack length from time-matched control group (Figure 4C) as a reference. **F**. Tissue stiffness comparisons at 95% culture length or -5% stretch (2-way ANOVA P = 0.0011). **G**. Tissue stiffness comparison at 9% stretch (SB-431542 P < 0.0001). **H**. Representative twitch from all groups at 1Hz pacing and 10% stretch. **I**. Normalized peak forces at 1Hz pacing and 10% stretch. Dashed line indicated the peak force from time-matched control group (Figure 5G) for reference (Mavacamten P = 0.0024, SB-431542 P = 0.0196). **J**. TTP at 1Hz pacing and 10% stretch (2-way ANOVA P = 0.01). Dashed line indicated the TTP from time-matched control group (Figure 5H) for reference. **K**. RT50 at 1Hz pacing and 10% stretch (2-way ANOVA P = 0.0003). **L**. Force-time integrals at 1Hz pacing and 10% stretch (Mavacamten P = 0.0353, SB-431532 P = 0.0009). 2-way ANOVA with planned comparisons (E, J, K) or Tukey's post hoc test (D, G, H) and 3-way ANOVA with repeated measures (C, F) were performed. * P < 0.05, ** P < 0.01, *** P < 0.001, **** P < 0.0001. All error bars are expressed as standard deviations.

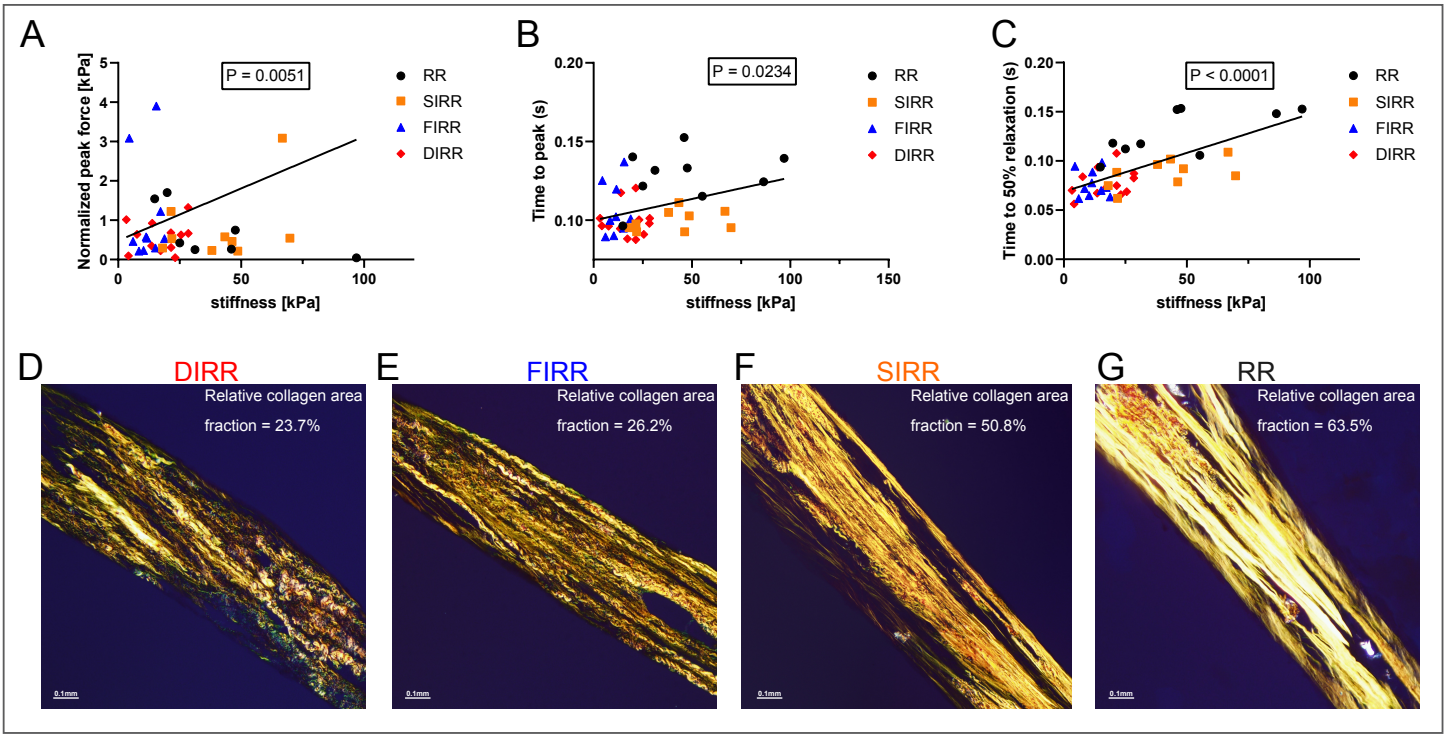

Figure 7. Matrix stiffness is highly correlated to EHT active mechanics.
A. Correlation between stiffness and peak force for aggregated data among all four groups at 10% stretch (total n = 41). **B**. Correlation between stiffness and TTP for aggregated data among all four groups. **C**. Correlation between stiffness and RT50 for aggregated data among all four groups. Linear regression analysis was performed for A-C. **D-G**. Representative polarized picrosirius red staining for total collagen content for DIRR, FIRR, SIRR, and RR tissues respectively, with 20x magnification and 12ms exposure time.

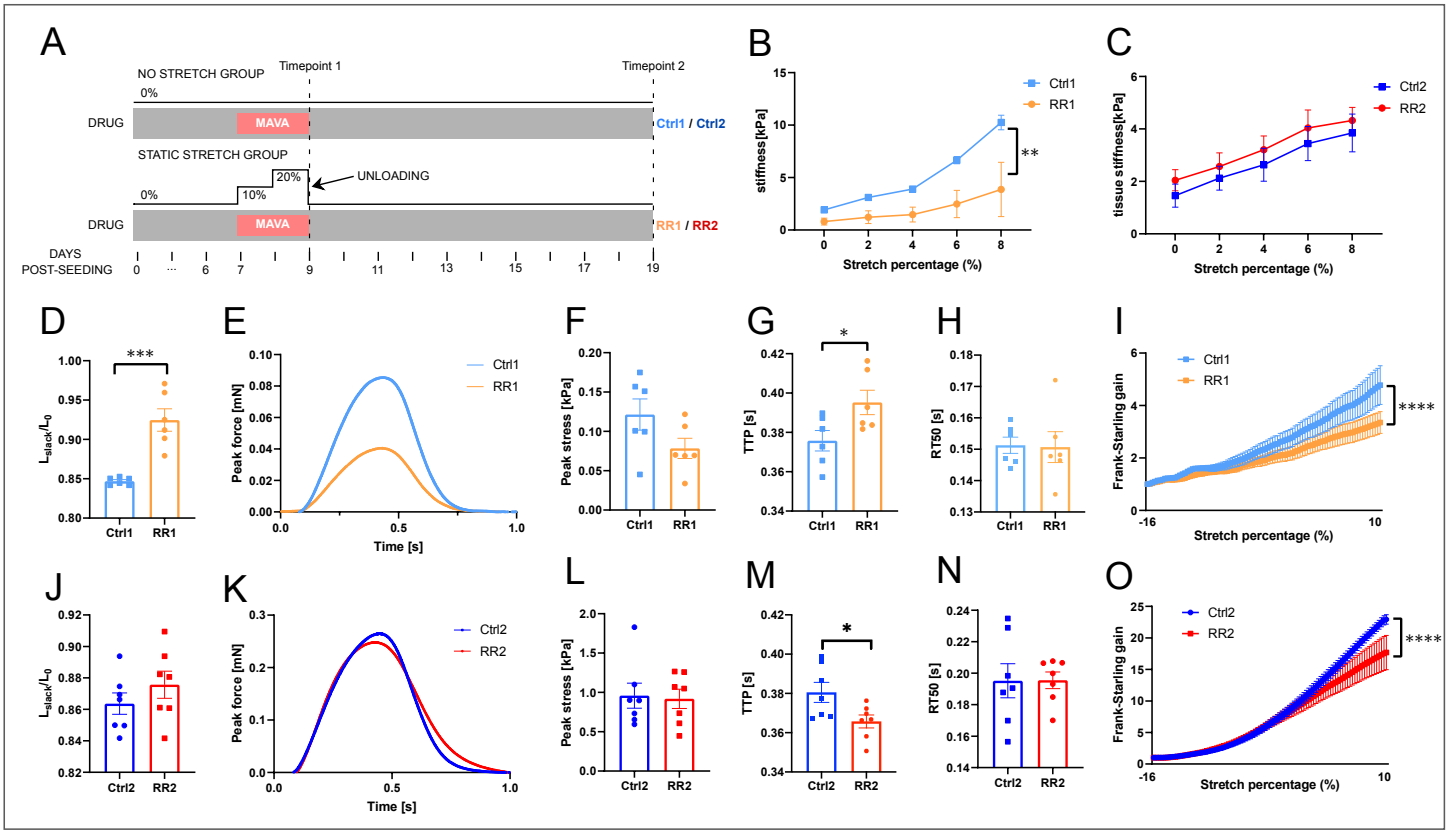

Figure 8. Reverse remodeling is observed and characterized in EHTs containing human iPSC-derived cardiomyocytes.
A. Schematic of the experimental design. A control group (Ctrl) was compared to a reverse remodeling (RR) group with static step-wise stretch immediately after unloading (timepoint 1) and 9 days post-unloading (timepoint 2). Ctrl1 tissue n = 6, Ctrl2 n = 7, RR1 n= 6, RR2 n = 7. Data in panels B, D-I were from timepoint 1, and C, J-O were from timepoint 2. All data were collected at 1Hz pacing. **B**. Stiffness of Ctrl1 and RR1 from 0 to 8% stretch ($P = 0.0028$). **C**. Stiffness of Ctrl2 and RR2 from 0 to 8% stretch. **D**. Slack lengths of Ctrl1 and RR1 ($P = 0.0003$). **E**. Representative active twitch of Ctrl1 adnd RR1 at 10% stretch. **F**. Peak stress of Ctrl1 and RR1 at 10% stretch. **G**. TTP of Ctrl1 and RR1 at 10% stretch ($P = 0.0374$). **H**. RT50 of Ctrl1 and RR1 at 10% stretch. **I**. Frank-Starling response of Ctrl1 and RR1 from -16% to 10% stretch ($P < 0.0001$). **J**. Slack lengths of Ctrl2 and RR2. **K**. Representative active twitch of Ctrl2 adnd RR2 at 10% stretch. **L**. Peak stress of Ctrl2 and RR2 at 10% stretch. **M**. TTP of Ctrl2 and RR2 at 10% stretch. **N**. RT50 of Ctrl2 and RR2 at 10% stretch. **O**. Frank-Starling response of Ctrl2 and RR2 from -16% to 10% stretch ($P < 0.0001$). Experiments were analyzed with two-tailed unpaired t tests (D, F, G, H, J, L, M, N), 2-way ANOVA with repeated measures (B, C, I, O). * $P < 0.05$, ** $P < 0.01$, *** $P < 0.001$, **** $P < 0.0001$. All error bars are expressed as standard deviations.

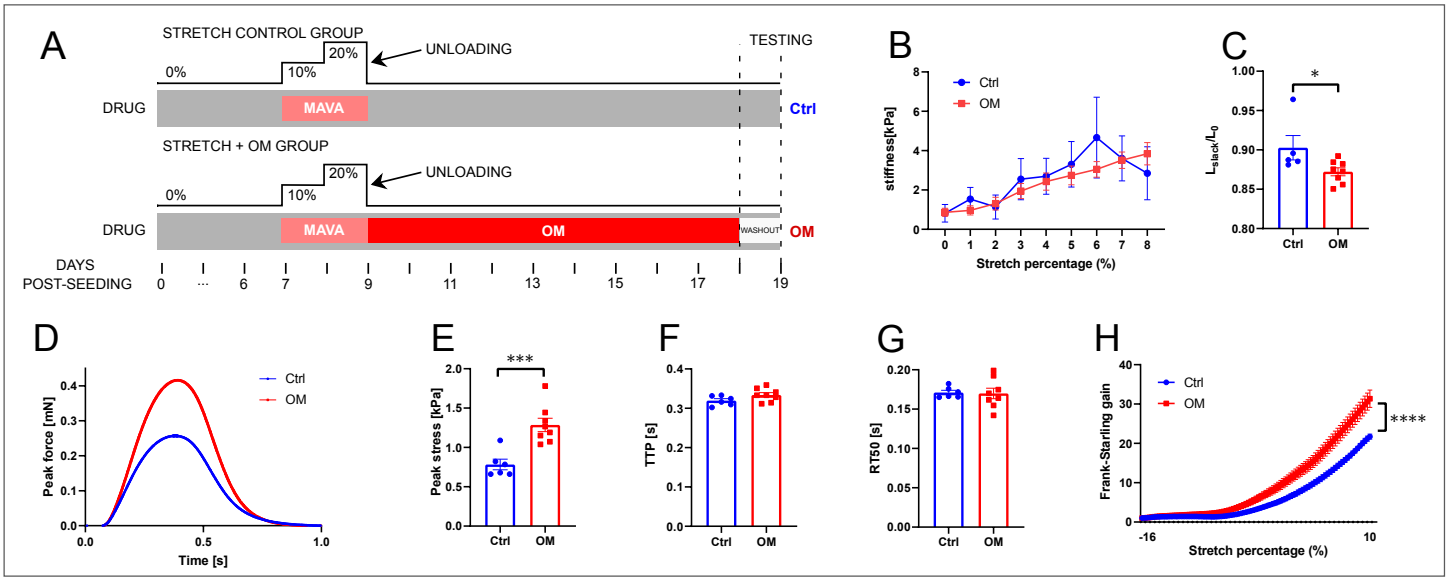

Figure 9. Omecamtiv Mecarbil (OM) enhances reverse remodeling in human EHTs.
A. Schematic of the experimental design. The control group (Ctrl, n = 6) consisted of the standard reverse remodeling protocol and was compared to 1 µM OM-treated reverse remodeling (OM, n = 8) group. Data were collected 9 days after unloading and 24-hr drug washout. Contractions were elicited by 1Hz pacing during data collection. **B**. Tissue stiffness from 0 to 8% stretch. **C**. Ctrl and OM group slack length (P = 0.0468). **D**. Representative active raw twitch of Ctrl and OM tissues. **E**. Peak stress at 10% stretch (P = 0.0009). **F**. TTP of Ctrl and OM tissues. **G**. RT50 of Ctrl and OM tissues. **H**. Frank-Starling response from -16% to 10% stretch (P < 0.0001). Experiments were analyzed with 2-way ANOVA with repeated measures (B, H) and two-tailed unpaired t tests (C, E, F, G). * P < 0.05, ** P < 0.01, *** P < 0.001, **** P < 0.0001. All error bars are expressed as standard deviations.